



HAL
open science

Soot Production and Radiative Heat Transfer in Opposed Flame Spread over a Polyethylene Insulated Wire in Microgravity

J. Orlac'h, A. Guibaud, J. Consalvi, J Orlac'H, J. Citerne, G. Legros

► **To cite this version:**

J. Orlac'h, A. Guibaud, J. Consalvi, J Orlac'H, J. Citerne, et al.. Soot Production and Radiative Heat Transfer in Opposed Flame Spread over a Polyethylene Insulated Wire in Microgravity. *Fire Technology*, Springer Verlag, 2020, 56, pp.287-314. 10.1007/s10694-019-00850-8 . hal-02279446

HAL Id: hal-02279446

<https://hal.sorbonne-universite.fr/hal-02279446>

Submitted on 5 Sep 2019

HAL is a multi-disciplinary open access archive for the deposit and dissemination of scientific research documents, whether they are published or not. The documents may come from teaching and research institutions in France or abroad, or from public or private research centers.

L'archive ouverte pluridisciplinaire **HAL**, est destinée au dépôt et à la diffusion de documents scientifiques de niveau recherche, publiés ou non, émanant des établissements d'enseignement et de recherche français ou étrangers, des laboratoires publics ou privés.

Soot Production and Radiative Heat Transfer in Opposed Flame Spread over a Polyethylene Insulated Wire in Microgravity

A. Guibaud, J. Consalvi, J. Orlac'h, J. Citerne, G. Legros

► **To cite this version:**

A. Guibaud, J. Consalvi, J. Orlac'h, J. Citerne, G. Legros. Soot Production and Radiative Heat Transfer in Opposed Flame Spread over a Polyethylene Insulated Wire in Microgravity. *Fire Technology*, Springer Verlag, 2019, 10.1007/s10694-019-00850-8 . hal-02279446

HAL Id: hal-02279446

<https://hal.sorbonne-universite.fr/hal-02279446>

Submitted on 5 Sep 2019


HAL is a multi-disciplinary open access archive for the deposit and dissemination of scientific research documents, whether they are published or not. The documents may come from teaching and research institutions in France or abroad, or from public or private research centers.

L'archive ouverte pluridisciplinaire **HAL**, est destinée au dépôt et à la diffusion de documents scientifiques de niveau recherche, publiés ou non, émanant des établissements d'enseignement et de recherche français ou étrangers, des laboratoires publics ou privés.



Soot Production and Radiative Heat Transfer in Opposed Flame Spread over a Polyethylene Insulated Wire in Microgravity

A. Guibaud, CNRS, UMR 7190, Institut Jean Le Rond d'Alembert, Sorbonne Université, Paris 75005, France

*J. L. Consalvi** , *IUSTI/UMR CNRS 7343, Aix-Marseille Université, 5 rue E. Fermi, Marseille Cedex 13 13453, France*

J. M. Orlac'h, CNRS, UMR 7190, Institut Jean Le Rond d'Alembert, Sorbonne Université, Paris 75005, France; Laboratoire EM2C, CNRS, Centrale Supélec, Université Paris-Saclay, Grande Voie des Vignes, Châtenay-Malabry Cedex 92295, France

J. M. Citerne, G. Legros, CNRS, UMR 7190, Institut Jean Le Rond d'Alembert, Sorbonne Université, Paris 75005, France

Received: 1 November 2018/**Accepted:** 22 March 2019

Abstract. Flame spread over an insulated electrical wire is identified as a fire scenario in space vehicles. In such microgravity configurations, the contribution of thermal radiation from gaseous participating species and soot to the wire burning rate and flame spread is not fully understood and the present paper addresses this question both experimentally and numerically. A non-buoyant opposed-flow flame spread configuration over a nickel–chrome wire coated by Low Density PolyEthylene (LDPE) is considered with an O_2/N_2 oxidizer composed of 19% of oxygen in volume and a flow velocity of 200 mm/s. Flame spread rate, pyrolysis rate, stand-off distance, soot volume fraction, and soot temperature are experimentally determined based on optical diagnostics that capture the flame spread in parabolic flights. The numerical model uses the measured spread and pyrolysis rates as input data and solves transport equations for mass, momentum, species, energy, and soot number density and mass fraction in an axisymmetric flame-fixed coordinate system in conjunction with a simple degradation model for the LDPE and a state-of-the-art radiation model. The model considers two assumptions. First, pure ethylene results from the decomposition of LDPE and, second, an acetylene/benzene based-soot model, initially validated for C_1 – C_3 hydrocarbons, can be extended with minor modifications to model soot production of LDPE. Comparisons between model predictions and experimental data in terms of flame structure and soot volume fraction support these assumptions. The major finding of this study is that radiation contributes negatively to the surface heat balance along the LDPE molten surface and the coating ahead of the molten front.

* Correspondence should be addressed to: J. L. Consalvi, E-mail: jean-louis.consalvi@univ-amu.fr

This shows that the convective heat transfer from the flame is the main contribution to sustain the pyrolysis process and the flame spread is mainly ensured owing to the combined contribution of convection from flame and conduction inside the condensed phase. The maximum incident radiative flux along the molten ball is 17.5 kW/m^2 and is reached at the molten ball trailing edge whereas the radiant fraction is about 0.25. Neglecting flame self-absorption affects these values by less than 5%, showing that the optically-thin approximation is valid for this flame. In addition, soot radiation dominates the radiative heat transfer in this flame, contributing for about two-third of the total radiation. Finally, model results show that the usually-used thermally-thin assumption throughout the LDPE coating is not strictly valid.

Keywords: Insulated wire, Opposed-flow flame spread, Microgravity, Soot production, Heat transfer

List of Symbols

a	Stretch function (–)
A_S	Soot surface area (m^{-1})
C_a	Agglomeration rate constant (–)
c	Heat capacity ($\text{J kg}^{-1} \text{K}^{-1}$)
f	k -distribution function (m^{-1})
f_S	Soot volume fraction (–)
g	Cumulative k -distribution function (–)
I_g, I	Radiative intensity ($\text{W m}^{-2} \text{sr}^{-1}$)
I_b	Blackbody intensity (Planck function) ($\text{W m}^{-2} \text{sr}^{-1}$)
k	Absorption coefficient variable (m^{-1})
k_B	Boltzmann constant (J kg^{-1})
L	Heat of reaction (J kg^{-1})
\dot{m}_{pyr}	Pyrolysis mass flow rate (kg s^{-1})
\dot{m}_{pyr}''	Pyrolysis mass flow rate per unit area ($\text{kg m}^{-2} \text{s}^{-1}$)
N_A	Avogadro number (part mol^{-1})
NC_{min}	Number of carbon atoms in the incipient soot particle (–)
N_S	Soot number density per unit mass of mixture (part kg^{-1})
\mathbf{n}_q	Unit surface normal (pointing away from surface into the medium)
q_{net}''	Net heat flux (W m^{-2})
q_R''	Radiative flux (W m^{-2})
$q_{R,inc}''$	Incident radiative flux (W m^{-2})
$q_{R,net}''$	Net radiative flux (W m^{-2})
$q_{R,R}''$	Surface re-radiation (W m^{-2})
r	Radial coordinate or radius (m)
\mathbf{r}	Position vector (m)
\hat{s}	Unit vector into a given direction (–)
T	Temperature (K)
u	Velocity (m s^{-1})
u_p	Spread rate (m s^{-1})
W_i	Molecular weight of the i th species (kg mol^{-1})
Y_i	Mass fraction of the i th species (–)
z	Axial coordinate (m)
δ	Stand-off distance (m)
$\Delta\eta_j$	Narrow band spectral resolution (cm^{-1})
η	Wavenumber (cm^{-1})
κ	Absorption coefficient (m^{-1})
λ	Thermal conductivity ($\text{W m}^{-1} \text{K}^{-1}$)
ρ	Density (kg m^{-3})

Soot Production and Radiative Heat Transfer in Opposed Flame Spread over

$\dot{\omega}_n$	Reaction rate for soot nucleation ($\text{mol m}^{-3} \text{s}^{-1}$)
$\dot{\omega}_{sg}$	Reaction rate for soot surface growth ($\text{mol m}^{-3} \text{s}^{-1}$)
$\dot{\omega}_{N_S}$	Reaction rate for soot number density ($\text{part m}^{-3} \text{s}^{-1}$)
$\dot{\omega}_{O_2}$	Reaction rate for soot oxidation by O_2 ($\text{kg m}^{-3} \text{s}^{-1}$)
$\dot{\omega}_{OH}$	Reaction rate for soot oxidation by OH ($\text{kg m}^{-3} \text{s}^{-1}$)
$\dot{\omega}_{Y_S}$	Source term for soot mass fraction ($\text{kg m}^{-3} \text{s}^{-1}$)
Ω_i	Solid angle around the direction s_i

Subscript

b	Molten ball
core	Metallic core
f	Flame
F	Fuel
g	Gas
inc	Incident
m	Molten phase
$melt$	Melting
mix	Mixing
pyr	Pyrolysis
PE	Polyethylene
R	Radiation or radiative
r	r -direction
ref	Reference state
S	Soot
wire	Coated wire
z	z -direction
η	At a given wavenumber or per unit wavenumber
∞	Ambient

Superscript

FS	Full spectrum
NB	Narrow band
g	Gas
$g-s$	Gas-soot

1. Introduction

Flame spread over an insulated electrical wire has been paid a special attention since unexpected overheating of wires by electrical current overshoots has been identified as a primary cause of fire initiation and growth in a space vehicle. Following the early work of Greenberg et al. [1], most of the experimental studies have considered flame spread in microgravity over thin electrical wires (diameter ~ 1 mm), made of a potentially flammable polymer coating and a metallic core, in quiescent or opposed flow configurations [2–6]. Kikuchi et al. [2] investigated experimentally the effects of several parameters, namely, ambient pressure and oxygen concentration, dilution gas, wire initial temperature, and diameter on the flame spread rate over ethylene-tetrafluoro-ethylene insulated wires. These authors found that spread rates in microgravity under preheating conditions are higher than in normal gravity whatever the oxygen concentration considered. In addition,

they showed that the spread rate increases as the wire diameter decreases. Fujita et al. [3] considered flame spread over PolyEthylene (PE)-insulated wires in an opposed flow. These authors identified the existence of four regimes as the flow velocity increases, namely, an oxygen transport control regime where the flame spread rate increases to reach a maximum, a geometrical effect regime where the flame spread rate decreases, a thermal regime where the flame spread rate is almost independent of the flow velocity, and a chemical kinetic control regime. In particular, the existence of the geometrical effect regime and a maximum spread rate at the transition between the oxygen transport control and geometrical effect regimes can be viewed as unique features of flame spread over wires. Citerne et al. [4] investigated interacting flame spreads as three parallel wires burn concomitantly. The flame was found to spread faster along the central wire and its corresponding mass loss rate was found to be higher than for a single wire. This effect was attributed to the radiative heat transfer from the lateral flames. Other experimental studies were reported with the objective of proposing standard flammability tests based on the limiting oxygen concentration (LOC) method, LOC being defined as the minimum oxygen volumetric fraction that supports the flame spread over the wire coating [5, 6].

As a matter of fact, the absence of buoyancy leads to enhanced residence times, favoring the soot production, therefore potentially increasing the radiative heat transfer [7, 8]. This in turn may affect the flame spread over materials [9]. Although meaningful studies reported on soot production processes and radiative heat transfer in non-buoyant flames [10–15], the previous literature survey reveals that these processes have not retained specific attention within the context of flame spread over insulated wires, soot production being even neglected in preliminary numerical efforts [16].

The objective of the present study is to investigate experimentally and numerically soot production and radiative heat transfer in flame spread over insulated wire in microgravity. Experiments were conducted in parabolic flights. The fields of soot volume fraction and temperature were measured by the Broadband Modulated Absorption Emission (BMAE) technique that has been recently developed [17]. The present paper first outlines the experimental setup and optical diagnostics to measure flame spread, stand-off distance, soot volume fraction, and temperature. The numerical model is then described. The subsequent results are finally presented and discussed.

2. Experiments

Experiments were conducted in parabolic flights which provide 22 s long sequences of microgravity with an accuracy level of $10^{-2} g_0$ ($g_0 = 9.81 \text{ m s}^{-1}$). A specific rig has been designed to enable the study of flame spread over LDPE coated wires in an opposed oxidizer flow [4]. This especially includes a combustion chamber where the pressure, the oxygen content, and the velocity of the oxidizer flowing along the samples can be controlled together with the power of the ignition device.

2.1. Experimental Setup

The experimental setup on board the aircraft consists of three sub-rigs that are extensively detailed in Ref. [4]. The central element of this setup is a cylindrical combustion chamber with an inner diameter of 190 mm. The gas flow is straightened at the entrance of the chamber to provide a flat velocity profile around the cylindrical samples located along the central axis of the chamber. Oxidizer flows can be generated with an oxygen content ranging from 0% to 21%, a pressure from 0.4 up to 1.5 bars, and a velocity between 0 mm s⁻¹ and 300 mm s⁻¹. In the present study, the oxidizer flow is set at an oxygen content of 19%, atmospheric pressure, and a velocity of 200 mm s⁻¹. The sample considered here is a LDPE-coated nickel–chrome (NiCr) wire. The diameter of the NiCr core, d_{core} , is 0.5 mm and the thickness of the insulation is 0.3 mm, leading to an outer diameter for the insulated wire, d_{wire} , of 1.1 mm. The sample length is 150 mm. Given the duration of each parabola and the velocities recorded in the opposed flow, this is more than three times the maximum propagation length expected. Consequently, border effects linked to heat conduction throughout the metallic core can be neglected. This configuration of polyEthylene cylinders formed around an inert core that could be heated electrically was widely considered from the early works of Ref. [18]. Experiments were performed by using NiCr but also other metals such as copper. Only experiments related to NiCr were found to lead to steady spread rates. Still, it is worth mentioning here that no existing or planned spacecraft uses NiCr wire or LPDE insulation.

The sample is ignited using a hot Kanthal wire, and images are captured using a JAI AT-140CL digital tri-CCD camera. A telecentric lens is mounted on the camera to limit the light collection to beams parallel to the optical axis. With this arrangement, the spatial resolution of the projected data is 76 μm for each spectral band and images are acquired at a rate of 34.67 fps. At this rate, a LEDs backlight behind the samples is alternatively set on and off, hence images are consecutively recorded with and without backlight all along every microgravity period. This imaging allows for the optical measurements specified below.

2.2. Experimental Measurements

From the frames obtained, flame spread rate, pyrolysis rate, and stand-off distance are determined using image processing. In addition, the Broadband Modulated Absorption Emission technique [17] is implemented to probe soot volume fraction and temperature fields from the frames captured within the visible spectrum. As the ignition procedure generates a transient state, the existence of a steady state propagation is first assessed by tracking the time history of several characteristic length scales captured by the camera. Taken together, the flame front, the flame length, but also the dimensions of a liquid ‘ball’ formed by the melted LDPE in the vicinity of the flame leading edge reflect the time evolution of the solid, liquid and gaseous phases hereby present. Once all these quantities only vary by amounts below the level of noise from the acquisition setup, the flame is assumed to spread steadily and the subsequent data analysis is performed.

2.2.1. *Flame Spread, Pyrolysis Rate, and Stand-off Distance* Figure 1 illustrates the procedures to determine flame spread, pyrolysis rate, and stand-off distance from the measurements. The flame spread rate, u_p , is evaluated by tracking the time evolution of the position of the luminous flame front as captured on the non-backlighted images (see Fig. 1c) for a recording period longer than 3 s. For each image, a threshold method is used to determine the position of the first row of pixel identified as the flame front. u_p is then extrapolated from a linear regression

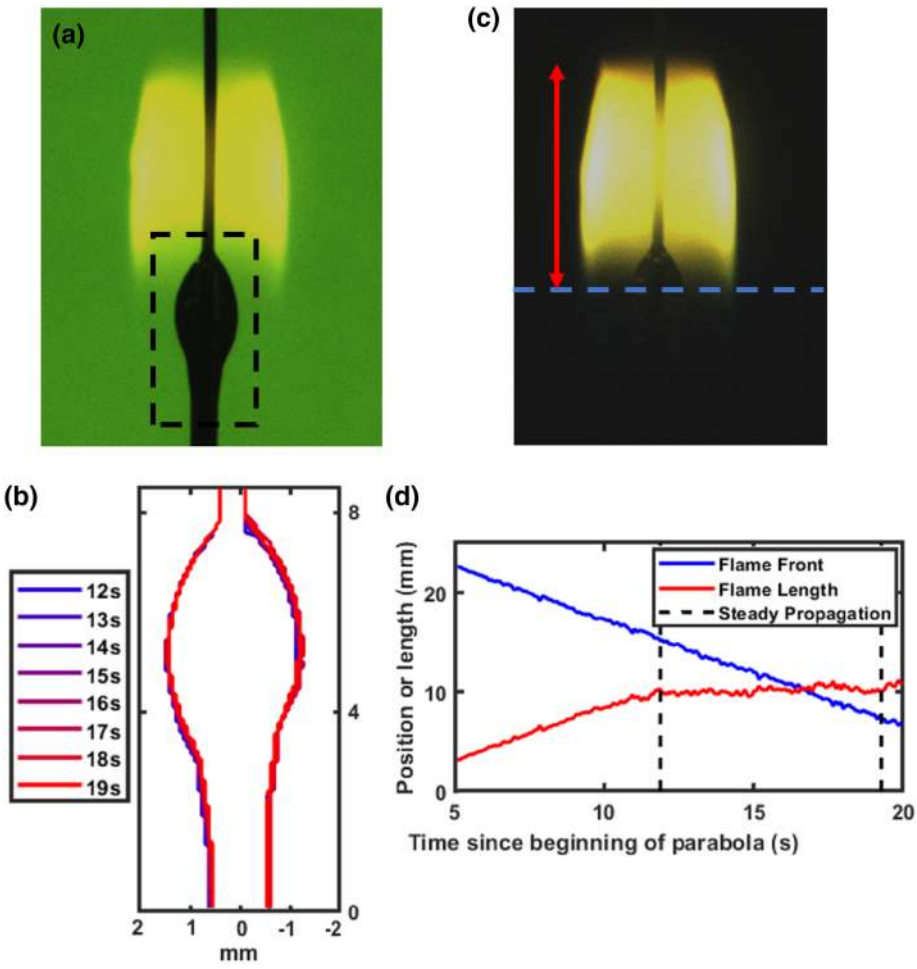


Figure 1. Details on the procedures to determine flame spread, pyrolysis rate and stand-off distance from the measurements: (a) typical backlighted frame and (b) set of wire contours extracted from this kind of frame; (c) typical unbacklighted frame and (d) evolution with time along a microgravity period of the flame front and length (indicated by the blue dotted line and the red double arrows on the unbacklighted frame, respectively) (Color figure online).

of the time evolution of the flame front location during the steady-state propagation. For consistency, the spread rate is considered correct only if the coefficient of determination of the regression is above 0.99.

The pyrolysis rate, \dot{m}_{pyr} , along the propagation at steady rate is evaluated from the spread rate and simple geometric considerations by assuming a constant density of the LDPE insulation of $\rho_{PE} = 0.92 \text{ kg m}^{-3}$:

$$\dot{m}_{pyr} = \rho_{PE} u_p \pi (r_{wire}^2 - r_{core}^2) \quad (1)$$

The stand-off distance, defined as the radial distance between the wire and the flame sheet, is evaluated through a similar procedure along the radial coordinate. It assumes that the soot luminous region on the rich side of this diffusion flame is immediately surrounded by the flame sheet [15].

For the conditions investigated, the steady propagation is 7 s long (see the period delineated by the dotted lines in Fig. 1d). Over that period, results show a flame spread rate, u_p , of 1.07 mm s^{-1} and a pyrolysis rate, \dot{m}_{pyr} , of 0.74 mg s^{-1} .

2.2.2. Soot Volume Fraction and Temperature Soot volume fraction and temperature fields are obtained using the B-MAE technique as extensively outlined in Ref. [17]. At a given time within the microgravity period, these fields can be computed provided four kinds of images: the flame with backlight, the backlight alone, the flame alone, and the background noise.

Fifty images featuring the flame with backlight and 50 images featuring the flame without backlight are averaged over the steady propagation period. For the flames to overlap on the images, they are shifted following the flame position recorded for the flame spread rate (see the superimposition in Fig. 1b). Background noise and backlight images are averaged over 50 frames recorded before the sample is ignited. Figure 2 illustrates the soot volume fraction, f_s , and temperature, T , fields recovered experimentally.

2.2.3. Experimental Error Assessment As images are averaged over a limited time of steady propagation, the repeatability of experimental measurements has to be assessed. Given the camera acquisition rate of 34.67 fps, a hundred images, alternatively backlit and unbacklit, correspond to roughly 3 s of steady propagation. Over the 7 s of steady propagation observed in the present case, there is some freedom to choose the initial dataset.

Consequently, results from four different sets of one hundred consecutive images are compared. Figure 3 illustrates the spatial distribution of soot volume fraction. The contour plot highlights positions with a soot volume fraction above 5 ppm. These distributions only differ of a few pixels, which illustrates the very similar soot location for these measurements. Yet, the slight difference in distribution from one measurement to another forbids a point by point comparison of soot volume fraction and temperature, as the profiles do not overlap perfectly. As a consequence, populations of soot temperature / volume fraction measurements in the flame are compared, for locations with soot volume fraction above 5 ppm.

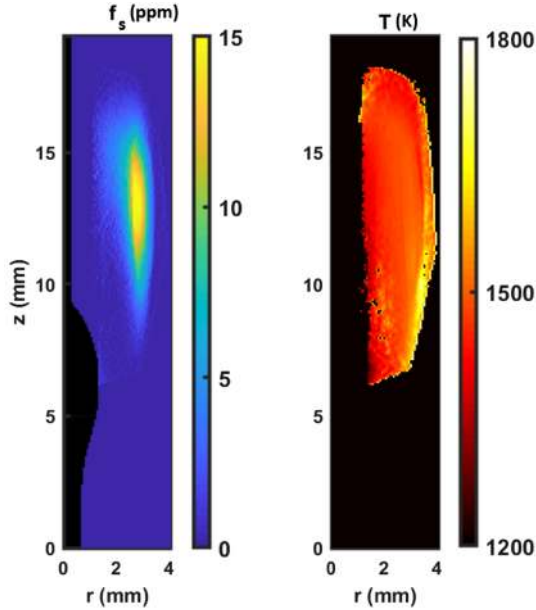


Figure 2. Fields measured by the B-MAE technique: (a) soot volume fraction; (b) temperature.

These results are displayed in Fig. 4. It can then be inferred that soot volume fraction is recovered with a precision of 1 ppm whereas temperature is determined with a precision of 50 K. Though they lead to an estimation of measurements precisions, such data do not specify which dataset must be retained. The ultimate choice is made by comparing the accelerometric data recorded in the same periods. The dataset presenting with the weaker g-jitters is then selected.

3. Numerical Model

3.1. Configuration and Assumptions

The configuration considered is that described in the previous section. The objective of this study is to provide a fine description of gas and soot radiation for steady spread rate. In order to address this problem, only modeling the gas phase processes is required and the spread rate, u_p , the pyrolysis rate, \dot{m}_{pyr} , and shape of the molten ball are specified as inputs from the experimental data. In the same manner, the solution of the heat transfer in the condensed phase is only required to specify proper boundary conditions for the gas phase.

The model solves the steady-state governing equations of both gaseous and condensed phases in axisymmetric coordinates. A flame-fixed coordinate system is considered so that the flame experiences an opposed forced flow of speed equal to the experimental spread rate (see Fig. 5). During the flame spread, a change in the volume of the molten insulation appears due to heat transfer from the flame, lead-

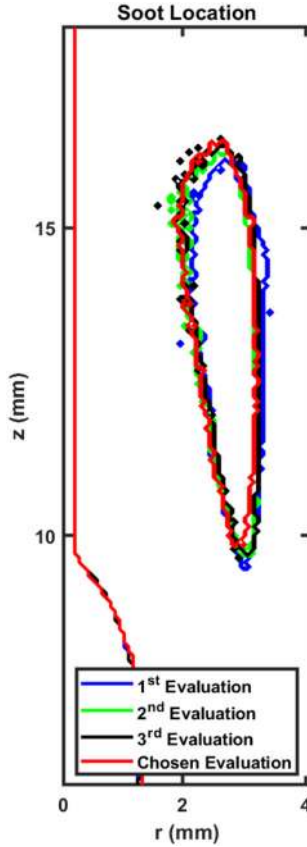


Figure 3. Comparison of physical distribution of soot volume fractions in the flame for four different datasets. The contours mark the positions with soot volume fractions above 5 ppm. The wire profile is visible on the left.

ing to the appearance of a “ball” (see Fig. 1a). This molten ball is assumed to delimit the pyrolysis region responsible for the fuel supply to the flame. A bare Nickel–Chrome core is then located downstream this ball whereas the unburnt coated wire is located upstream (see Fig. 5). The pyrolysis process is treated as a phase transition with the ball surface temperature being assumed to be at a pyrolysis temperature, T_{pyr} , and the pyrolysis mass flow rate per unit area, \dot{m}''_{pyr} , being related to the net heat flux to the surface, \dot{q}''_{net} , by $\dot{m}''_{pyr} = \dot{q}''_{net}/L_{pyr}$, where L_{pyr} is the pyrolysis heat of molten LDPE. In addition, the fuel injection velocity profile, $u_F(z)$, is deduced from measured fuel mass flow rate, \dot{m}_{pyr} , ball surface, S_b , and stand-off distance, $\delta(z)$. The analysis is based on the classical result of the reactive-laminar boundary layer theory, showing that the pyrolysis mass flow rate per unit area, \dot{m}''_{pyr} , is inversely proportional to the stand-off distance [19]:

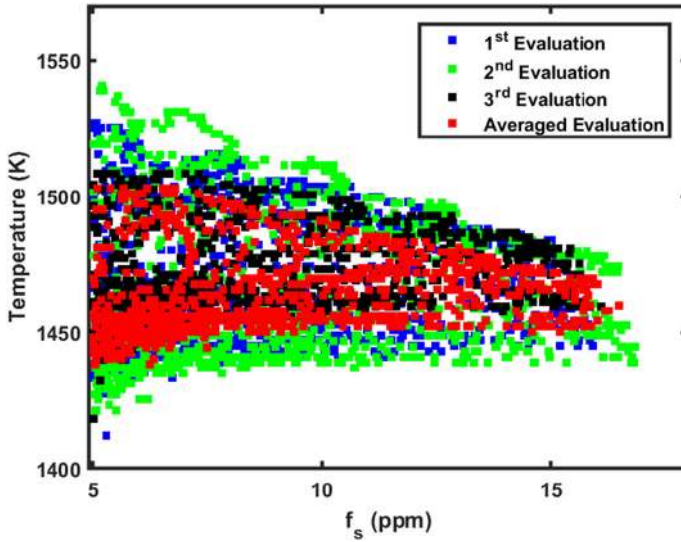


Figure 4. Comparison of experimental measurements in the (f_s, T) plan. From this graph, it can be assumed that B-MAE recovers soot volume fraction with a precision of 1 ppm and temperature with a precision of 50 K.

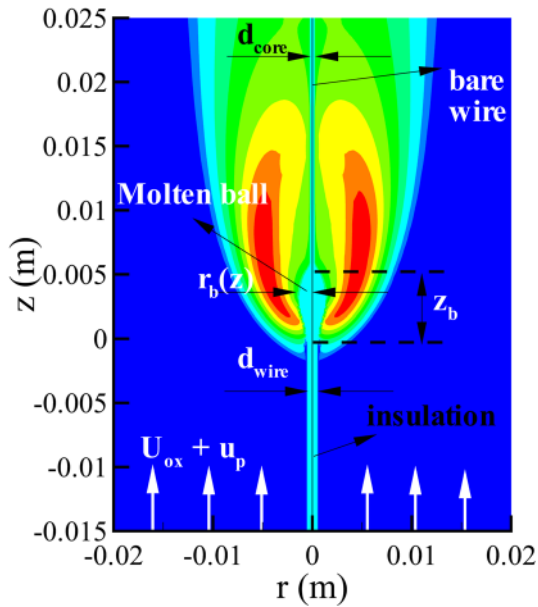


Figure 5. Computational details and notations. The computed fields of temperature is also plotted with the wire being represented by the lightest blue (Color figure online).

$$\dot{m}_{pyr}'' = \frac{C}{\delta(z)} = \rho_F u_F(z) \quad (2)$$

C is a constant which can be computed from:

$$C = \dot{m}_{pyr} / \int_0^{z_b} \frac{2\pi r_b(z)}{\delta(z)} dz \quad (3)$$

where $r_b(z)$ and z_b are the radial and axial locations of the ball surface and are determined experimentally (see Fig. 5). The fuel injection velocity profile, $u_F(z)$, is then determined from Eq. (2).

The conjugated heat and mass transfer between the gas phase and the condensed phase is solved by using a blocked-off region procedure [20]. In this procedure, the computational domain includes both gas and condensed regions. The standard numerical scheme is modified to render hydro-dynamically inactive the condensed regions and to correctly match the interface conditions at the burning or inert surface. At the gas-condensed phase interface, the mesh size is sufficiently refined to match accurately the ball surface. It should be recalled that the ball surface is taken from the experimental results.

3.2. Condensed Phase

As shown in Fig. 5, the condensed phase can be divided into three regions: (1) an unburnt insulated wire located ahead of the pyrolysis front ($z \leq 0$), (2) the molten ball where pyrolysis occurs ($0 < z \leq z_b$), and (3) the bare nickel–chrome core ($z > z_b$). As discussed previously, this study aims to provide an accurate description of the gas phase to characterize soot production and radiative heat transfer toward the condensed phase. As such the modeling of the heat and mass transfer processes within the condensed phase only intends to provide realistic boundary conditions for the gas-phase modeling, especially for $z \leq 0$ and $z > z_b$.

The surface of the Nickel–Chrome core exchanges heat with the gas-phase for $z > z_b$ and with the insulation for $z \leq z_b$. As a consequence, the heat transfer equation for the core is solved with the corresponding boundary conditions:

$$\rho_{core} c_{core} \frac{\partial T_{core}}{\partial t} + \rho_{core} c_{core} u_p \frac{\partial T_{core}}{\partial z} = \lambda_{core} \frac{\partial^2 T_{core}}{\partial z^2} + \frac{\lambda_{core}}{r} \frac{\partial}{\partial r} \left(r \frac{\partial T_{core}}{\partial r} \right) \quad (4a)$$

$$z \leq z_b : \lambda_{core} \frac{\partial T_{core}}{\partial r} \Big|_{r=r_{core}} = \lambda_{PE} \frac{\partial T_{PE}}{\partial r} \Big|_{r=r_{core}} \quad (4b)$$

$$z > z_b : \lambda_{core} \frac{\partial T_{core}}{\partial r} \Big|_{r=r_{core}} = \lambda_g \frac{\partial T_g}{\partial r} \Big|_{r=r_{core}} + \varepsilon_{Ni} \left(\dot{q}_{R,inc}'' - \sigma T_{core}^4(r = r_{core}, z) \right) \quad (4c)$$

$$\forall z : \left. \frac{\partial T_{core}}{\partial r} \right|_{r=0} = 0 \quad (4d)$$

The proposed model for the LDPE is based on the following assumptions: (1) the pyrolysis process is assumed to behave as a phase transition occurring at the ball surface (see Fig. 5). As a consequence, the ball surface temperature is equal to a fixed temperature, T_{pyr} , and there is no mass transfer within the polymer; (2) the melting process is also assumed to be a phase-transition. It occurs then at a fixed temperature, T_{melt} , and is characterized by a heat of melting, L_{melt} . During the melting stage, the heat capacity and the thermal conductivity (c_{melt} and λ_{melt} respectively) are computed using a mass-weighted average between the properties of virgin LDPE (denoted by the index v) and those of the molten LDPE (denoted by the index m). The heat transfer equation and the corresponding boundary conditions can be written as follows:

$$T_{PE} < T_{melt} : \rho_{PE} c_v \frac{\partial T_{PE}}{\partial t} + \rho_{PE} c_v u_p \frac{\partial T_{PE}}{\partial z} = \lambda_v \frac{\partial^2 T_v}{\partial z^2} + \frac{\lambda_v}{r} \frac{\partial}{\partial r} \left(r \frac{\partial T_{PE}}{\partial r} \right) \quad (5a)$$

$$T_{PE} = T_{melt} : \rho_{PE} c_{melt} u_p \frac{\partial T_{PE}}{\partial z} = \lambda_{melt} \frac{\partial^2 T_{PE}}{\partial z^2} + \frac{\lambda_{melt}}{r} \frac{\partial}{\partial r} \left(r \frac{\partial T_{PE}}{\partial r} \right) + \dot{m}_{melt}''' L_{melt} \quad (5b)$$

$$T_{PE} > T_{melt} : \rho_{PE} c_m \frac{\partial T_{PE}}{\partial t} + \rho_{PE} c_m u_p \frac{\partial T_{PE}}{\partial z} = \lambda_m \frac{\partial^2 T_{PE}}{\partial z^2} + \frac{\lambda_m}{r} \frac{\partial}{\partial r} \left(r \frac{\partial T_{PE}}{\partial r} \right) \quad (5c)$$

$$0 < z \leq z_b : T_{PE}(r = r_b, z) = T_{pyr} \quad (5d)$$

$$z < 0 : \lambda_{PE} \left. \frac{\partial T_{PE}}{\partial r} \right|_{r=r_{wire}} = \lambda_g \left. \frac{\partial T_g}{\partial r} \right|_{r=r_{wire}} + \varepsilon_{PE} \left(\dot{q}_{R,inc}'' - \sigma T_{PE}^4(r = r_{wire}, z) \right) \quad (5e)$$

$$-\infty < z \leq z_b : \lambda_{core} \left. \frac{\partial T_{core}}{\partial r} \right|_{r=r_{core}} = \lambda_{PE} \left. \frac{\partial T_{PE}}{\partial r} \right|_{r=r_{core}} \quad (5f)$$

The material properties adopted in this study are given in Table 1.

3.3. Gas Phase

3.3.1. Governing Equations The governing equations are briefly described here and more details can be found in Ref. [23]. The numerical model was initially developed to simulate laminar axisymmetric diffusion flames at normal gravity. The micro-gravity conditions are obtained when suppressing the gravitational force in the

Table 1
Properties of the Insulation Materials

c_v^a (J/kg/K)	c_m^a (J/Kg/K)	λ_v^a (W/m/K)	λ_m^a (W/m/K)	T_{pyr}^b (K)	T_{melt}^b (K)	L_{melt}^c (J/g)	ε_{PE} (-)
2300	2900	0.33	0.45	760	403	286	1

The density is computed as $\rho_{PE} = 948.2 - 0.94(T_{PE} - T_\infty)$ [16]

^aTaken from [21]

^bTaken from [16]

^cTaken from [22]

momentum equation. The numerical model includes the solution of the overall continuity equation, the Navier–Stokes equations in the low Mach number formulation, and transport equations for gas-phase species mass fractions and energy. Although LDPE vaporizes as higher molecular weight oligomers rather than monomer [24], the present study adopts the widely used assumption that pure ethylene is released from the pyrolysis of the LDPE [16, 25, 26]. The oxidation of ethylene was modeled by using the full chemical kinetic scheme developed by Qin et al. [27] which consists of 70 species and 463 reactions.

The conservation equations are solved in axisymmetric cylindrical coordinates using a finite volume method and the SIMPLE algorithm. Details of the discretization method and the strategy for handling the stiffness of the equation system can be found in previous publications [23].

3.3.2. Soot Model Soot is modeled by using an acetylene/benzene-based two-equation model [28]. It assumes that soot particles are locally spherical and monodisperse. Consequently, the soot particle dynamics can be described considering only two transport equations: one for the soot number density per unit mass of mixture (N_s), and another for the soot mass fraction (Y_s):

$$\frac{\partial \rho_g Y_s}{\partial t} + \frac{1}{r} \frac{\partial (r \rho_g u_{g,r} Y_s)}{\partial r} + \frac{\partial (\rho_g u_{g,z} Y_s)}{\partial z} = \frac{1}{r} \frac{\partial (r \rho_g V_{T,r} Y_s)}{\partial r} + \frac{\partial (\rho_g V_{T,z} Y_s)}{\partial z} + \dot{\omega}_{Y_s} \quad (6)$$

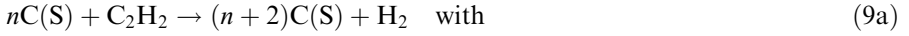
$$\frac{\partial \rho_g N_s}{\partial t} + \frac{1}{r} \frac{\partial (r \rho_g u_{g,r} N_s)}{\partial r} + \frac{\partial (\rho_g u_{g,z} N_s)}{\partial z} = \frac{1}{r} \frac{\partial (r \rho_g V_{T,r} N_s)}{\partial r} + \frac{\partial (\rho_g V_{T,z} N_s)}{\partial z} + \dot{\omega}_{N_s} \quad (7)$$

where $V_{T,r}$ and $V_{T,z}$ are the particle thermophoretic velocities in r and z directions, respectively [23].

The source term, $\dot{\omega}_{Y_s} = (\dot{\omega}_n + \dot{\omega}_{sg})W_s - \dot{\omega}_{O_2} - \dot{\omega}_{OH}$, for the soot mass fraction accounts for the contributions of soot nucleation, surface growth, and oxidation by O_2 and OH. The nucleation and surface growth processes are expressed as follows:



$$\dot{\omega}_n = 2k_1(T_g)[\text{C}_2\text{H}_2] + 6k_1'(T)[\text{C}_6\text{H}_6] \quad (\text{mol m}^{-3} \text{ s}^{-1}) \quad (8b)$$



$$\dot{\omega}_{sg} = 2k_2(T_g)A_S[\text{C}_2\text{H}_2] \quad (\text{mol m}^{-3} \text{ s}^{-1}) \quad (9b)$$

In these reactions [Eqs. (8a–9b)], C(S) represents carbon in its solid form, while $[\text{C}_2\text{H}_2]$ and $[\text{C}_6\text{H}_6]$ are the molar concentrations of acetylene and benzene, respectively. The parameters adopted for the nucleation and the surface growth processes are those provided by Lindstedt [28] in the initial formulation, then used and validated in Ref. [29] in axisymmetric laminar diffusion flames fueled by C₁–C₃ hydrocarbons, except for the pre-exponential factor for surface growth that was scaled here by a factor of 1.3 to match the soot production of LDPE. This scaling strategy is similar to that proposed by Moss and Aksit [30]. The parameters related to soot formation processes are reported in Table 2.

The rate of oxidation by O₂ was computed with the Nagle and Strickland-Constable (NSC) model [31], while oxidation rates by OH were based on the Fenimore and Jones model [32]. Collision efficiency factors of $\varphi_{OH} = 0.13$ was considered. The source term, $\dot{\omega}_{Ns}$, for the soot number density is given by Eq. (10):

$$\dot{\omega}_{Ns} = \frac{N_A}{NC_{min}} \dot{\omega}_n - 2C_a \left(\frac{6W_S}{\pi\rho_S} \right)^{1/6} \left(\frac{6k_B T_g}{\rho_S} \right)^{1/2} \left(\frac{\rho_g Y_S}{W_S} \right)^{1/6} (\rho_g N_S)^{11/6} \quad (10)$$

NC_{min} and C_a are taken equal to 60 and 9, respectively [28]. The soot density, ρ_S , was set to 2000 kg m⁻³ [28].

3.3.3. Radiation Model The spectral coverage range considered in the present study is 50–11,250 cm⁻¹. All the line data for CO₂ and H₂O used to generate the

Table 2
Reaction Rate Constants for Soot Formation, Following an Arrhenius Expression $k_j = A \exp(-T_a/T)$ (Units in K, m, s)

k_j	A	T_x	References
k_1	0.63×10^4	21,100	[28]
k_1'	0.75×10^5	21,100	[28]
k_2	0.75×10^{3a}	12,100	[28]

^aA scaling factor of 1.3 was applied to the expression for k_2 derived by Lindstedt [28]

databases described below are taken from HITEMP 2010 [33]. The Rayleigh's theory with the refraction indexes of Chang and Charalampopoulos [34] is applied to obtain the soot absorption coefficient.

The Full-Spectrum Correlated- k model is used as a gas radiative property model [35]. The method consists in reordering the absorption coefficient over the entire spectrum by introducing a Full Spectrum (FS) Planck-function weighted- k distribution, $f(T, \underline{\phi}, k)$, and a FS Planck-function weighted cumulative k -distribution, $g(T, \underline{\phi}, k)$. $\underline{\phi}$ is an array of state variables affecting the absorption coefficient, i.e. the temperature, the molar concentrations of the radiatively participating gaseous species, x_i , the total pressure, P , and the soot volume fraction, f_S . These two functions are defined as:

$$f(T, \underline{\phi}, k) = \frac{\int_0^\infty I_{b\eta}(T) \delta[k - \kappa_\eta(\underline{\phi})] d\eta}{I_b(T)} \quad (11a)$$

$$g(T, \underline{\phi}, k) = \int_0^k f(T, \underline{\phi}, k') dk' \quad (11b)$$

Due to the smooth nature of the cumulative function, the integration of the reordered wavenumber can be easily achieved with a simple integration scheme.

The FS Radiative Transfer Equation (RTE) and the spectrally integrated intensity, I , are expressed as [35]:

$$\frac{dI_g}{ds} = \hat{s} \cdot \nabla I_g(\mathbf{r}, \hat{s}) = k^*(T_{ref}, \underline{\phi}, g_{ref}) [a(T, T_{ref}, g_{ref}) I_b(T) - I_g(\mathbf{r}, \hat{s})] \quad \text{with} \quad (12a)$$

$$a(T, T_{ref}, g_{ref}) = \frac{dg(T, \underline{\phi}_{ref}, k)}{dg_{ref}(T_{ref}, \underline{\phi}_{ref}, k)} \quad (12b)$$

$$I(\mathbf{r}, \hat{s}) = \int_0^1 I_g(\mathbf{r}, \hat{s}) dg_{ref} \quad (12c)$$

In this study a 10-point Gauss quadrature scheme is used, leading to:

$$I(\mathbf{r}, \hat{\mathbf{s}}) \approx \sum_{i=1}^{N_G=10} I_{gi}(\mathbf{r}, \hat{\mathbf{s}}) \omega_i \quad (12d)$$

where N_G is the number of Gauss point and g_i and ω_i are a quadrature point and the corresponding weight.

The reference state is defined here by the molar fractions of the gas species averaged over the flame volume. The reference temperature is calculated as an emission weighted temperature [36].

A simple and efficient FS database was developed. Values of k^* ($T_{ref}, \underline{\phi}, g_{ref}$) and a ($T_{ref}, \underline{\phi}, g_{ref}$) are stored at the 10 Gauss points used to solve the FS RTE [Eq. (12a)] for different mixtures of CO_2 and H_2O . For each Gauss point, k^* and g are stored in the database for 6 values of x_{CO_2} , 6 values of $x_{\text{H}_2\text{O}}$, 6 values of f_s , 28 values of the gas temperature, T , and 28 values of the reference temperature, T_{ref} . At each grid point and for each quadrature point, linear interpolation on x_{CO_2} , $x_{\text{H}_2\text{O}}$, f_s and spline interpolation on T and T_{ref} are performed to obtain the k^* and a values at the desired conditions.

The FS database is generated from a NB k-distributions database itself generated from HITEMP 2010 [33]. In this NB database, the spectrum is divided into 450 NB with a resolution of $\Delta\eta_j = 25 \text{ cm}^{-1}$. For each NB, the NB k-g distributions were stored in the database for 128 values of g corresponding to a 128-point Gauss quadrature scheme, 6 mol fractions ranging between 0 and 1 (0, 0.1, 0.25, 0.5, 0.75, 1) for both CO_2 and H_2O , 38 temperatures ranging from 300 K to 4000 K (by a uniform step of 100 K). For each local state $\underline{\phi}$, the following procedure is used to determine the FS-K distribution. For each NB, a mixed NB distribution, $g_{mix}^{NB,g} - k_{mix}$ is then obtained by using the mixing scheme of Modest and Riazzi [37]:

$$g_{mix}^{NB,g}(k_{mix}) = \int_{g_{\text{CO}_2}=0}^1 \int_{g_{\text{H}_2\text{O}}=0}^1 H[k_{mix} - (k_{\text{CO}_2} + k_{\text{H}_2\text{O}})] dg_{\text{CO}_2} dg_{\text{H}_2\text{O}} \quad (13)$$

where H is the Heaviside function. The NB k-distribution of the gas-soot mixture ($g_{mix}^{NB,g-s} - k_{mix}$) is then obtained by adding the NB soot absorption coefficients to the narrow-band gas k-distribution over each narrow-band [37]. The FS $g_{mix}^{FS,g-s} - k_{mix}$ distributions are then assembled from the NB $g_{mix}^{NB,g-s} - k_{mix}$ distributions by using the following relationship [37]:

$$g_{mix}^{FS,g-s}(T, \underline{\phi}, k_{mix}) = \sum_{j \in [\text{allNBs}]} \frac{I_{bj}(T)}{I_b(T)} g_{mix}^{NB,g-s}(T, \underline{\phi}, k_{mix}) \quad \text{with} \quad (14a)$$

$$I_{bj} = I_{b\eta} \Delta\eta_j. \quad (14b)$$

The radiative transfer equation [Eq. (12a)] is solved by the Finite Volume Method (FVM) using the mapping developed by Chui et al. [38] for axisymmetric configurations. In this method the dependence of radiative intensity on two space coordinates and two angles is transformed into three space coordinates and one angle. Computations are carried out using the first-order UPWIND spatial discretization scheme and an angular mesh with 12×16 control angles. In this approach, a finite volume method discretization is employed for the spatial domain, leading to control volumes, V_p , of center \mathbf{r}_p . Similar to the spatial domain, the directional domain of 4π is broken up into n solid angles, Ω_i , of average direction, $\mathbf{s}_i = \int_{\Omega_i} \hat{s} d\Omega$, which exactly fill the directional domain without overlap [36]. The solution of the discretized radiative transfer equation leads to the radiative intensity at each control volume center and average direction, $I(\mathbf{r}_p, \mathbf{s}_i)$. The incident radiative flux at a point \mathbf{r}_p on a surface of normal \mathbf{n}_q pointed out of the surface is then computed as:

$$\dot{q}_{R,inc}''(\mathbf{r}_p) = \sum_{i/\mathbf{s}_i \cdot \mathbf{n}_q < 0} I(\mathbf{r}_p, \mathbf{s}_i) |\mathbf{s}_i \cdot \mathbf{n}_q|. \quad (15)$$

3.3.4. *Boundary Conditions* The boundary conditions are given in Table 3.

3.4. Computational Details

2D axisymmetric simulations are considered with an overall computational domain of 4 cm (r) \times 6 (z) cm. The computational domain is divided into 167 (r) \times 327 (z) cells by using a non-uniform grid. The finest resolution (76 μm \times 76 μm) is located at vicinity of the molten ball. The finest resolution includes the flame leading edge since the flame stabilization in this region may affect the region downstream [39]. In the solution of the radiative transfer equation, all the boundaries including the solid are assumed to be black, which is mainly justified by the strong deposition of soot on the wire.

Table 3
Boundary Conditions

Solid wall	$z < 0; r = r_{wire}; u_r = 0; u_z = u_p; \partial P / \partial n = 0; T = T_{PE}; \partial Y_i / \partial n = 0$ $z > z_b; r = r_{core}; u_r = 0; u_z = u_p; \partial P / \partial n = 0; T = T_{Ni}; \partial Y_i / \partial n = 0$ $0 \leq z \leq z_b; r = r_b; u_r = u_F; u_z = u_p; \partial P / \partial n = 0; T = T_{pyr}; \dot{m}_{pyr}'' = \dot{m}_{pyr}'' Y_{C_2H_4} - \rho D \frac{\partial Y_{C_2H_4}}{\partial r}$
Inflow (z = – 0.03 m)	$u_r = 0; u_z = U_{ox} + u_p; \partial P / \partial n = 0; T = T_\infty; Y_i = Y_{O_2}; Y_i = Y_{N_2}$
Outflow (z = 0.03 m)	$\partial u_r / \partial z = \partial u_z / \partial z = \partial T / \partial z = \partial Y_i / \partial z = 0; P = P_\infty$
Outflow (r = 0.04 m)	$\partial u_r / \partial r = \partial u_z / \partial r = \partial T / \partial r = \partial Y_i / \partial r = 0; P = P_\infty$

The notations are given in Fig. 5

4. Results and Discussions

4.1. Flame Structure and Comparison with Available Experimental Data

Figure 6 shows the computed (on the left) and measured (on the right) fields of temperature (top) and soot volume fraction (bottom). In addition, computed streamlines are plotted on the temperature diagram. Consistently with the measurement technique, the experimental temperature is only available for regions where significant amounts of soot are present.

Figure 6a₁ shows that the computed flame structure is typical of a reactive laminar boundary layer with the diffusion flame being attached close to the molten ball leading edge. The reaction zone extends downstream the ball trailing edge due to an excess of pyrolysate. The computed flame length, defined as the furthest axial location of the isotherm 1500 K, is 16.7 mm. The value of 1500 K was selected since it is expected to correspond to a threshold below which soot ceases to be oxidized [40, 41]. The radial location of the reaction zone (defining the stand-off distance), characterized by the highest temperature met at the location z considered, increases first from the flame leading edge to about $z = z_b$, remains approximately constant between $z = z_b$ and $z = 12.5$ mm, and decreases rapidly downstream. The streamlines closest to the condensed phase surface flows through the reaction zone whereas those released in upper locations are slightly deflected upwards by the flame and flows above the reaction zone.

Figure 6b₁ shows that, as expected, the soot is located in the fuel rich part of the flame. The soot volume fraction increases between $z = 5$ mm and $z = 11$ mm, reaches a peak equal to 14.8 ppm and is then oxidized as the reaction zone falls down to the wire. Contrasting Fig. 4b₁, b₂ shows that the computed soot field is consistent with the experimental one in terms of location, shape, and maximum value. Nevertheless, it can be observed that the size of the region of highest soot volume fraction is underestimated by the model. In addition, the soot is fully oxidized above $z \approx 1.3$ cm in the experiments whereas this occurs above $z \approx 1.6$ cm for the model, which suggests that the model underestimates soot oxidation.

Figure 7 shows computed and measured radial profiles of soot volume fraction at different locations along the wire in order to make quantitative comparisons. The model reproduces rather well the experimental profiles whatever the location considered. The shape of the profiles as well as the peak value are properly predicted despite some underestimation in the soot growth region ($z = 5$ mm and $z = 7.5$ mm) and overestimation in the soot oxidation region ($z = 12.5$ mm). However, at each location along the wire axis, the computed peak occurs at higher values of r and the soot region is shifted downstream as compared to the experiments. Radial temperature profiles at the same axial locations are plotted in Fig. 8. As discussed previously, experimental temperature is only available in the parts of the flame where significant amounts of soot are present, i.e. in the fuel rich region. Model predictions are in decent agreement with the experimental data. The largest discrepancies are observed at $z = 5$ mm for $r < 2$ mm.

For a given value of z , the stand-off distance represents the distance between the condensed phase surface and the radial location of the reaction zone. In the

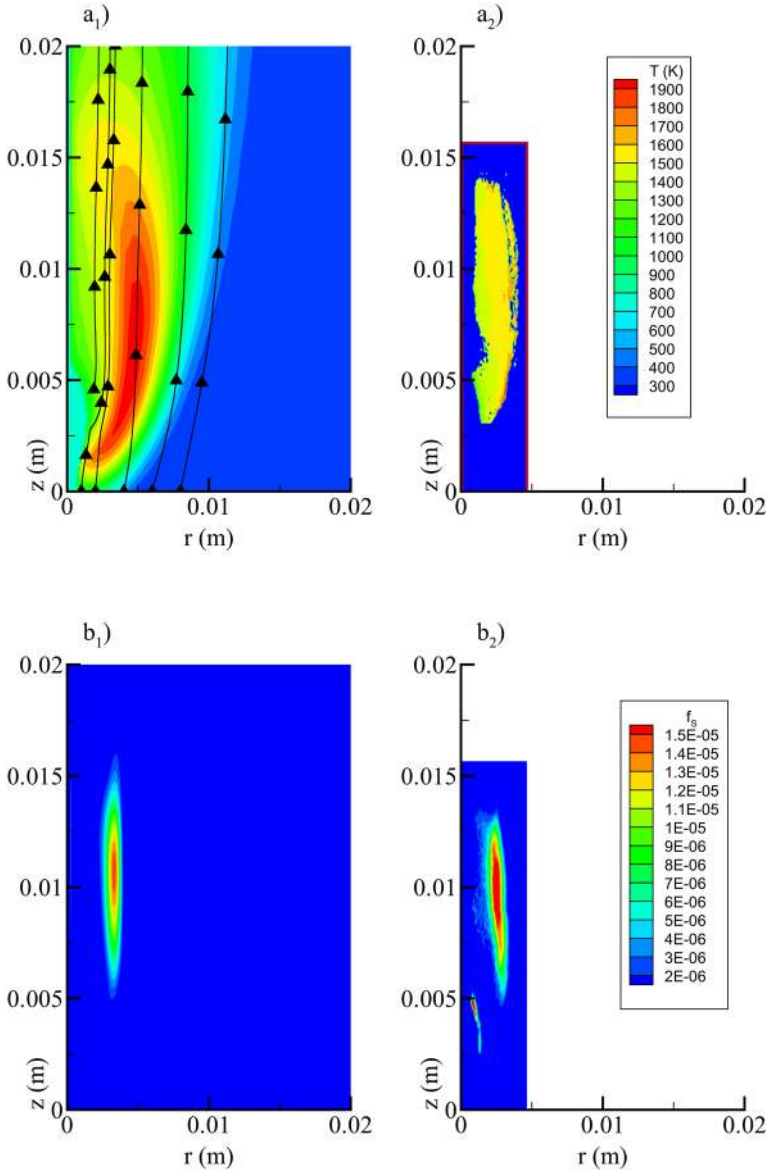


Figure 6. Computed and experimental fields of temperature (a) and soot volume fraction (b). The index 1 (left row) refers to simulations whereas the index 2 (right row) refers to experimental data.

experiments, the location of the reaction zone is defined as the furthest radial location of the luminous region. This is expected to correspond to the soot oxidation region [15]. On the numerical point of view, two definitions of the reaction zone are adopted: one based on the temperature peak and another one based on

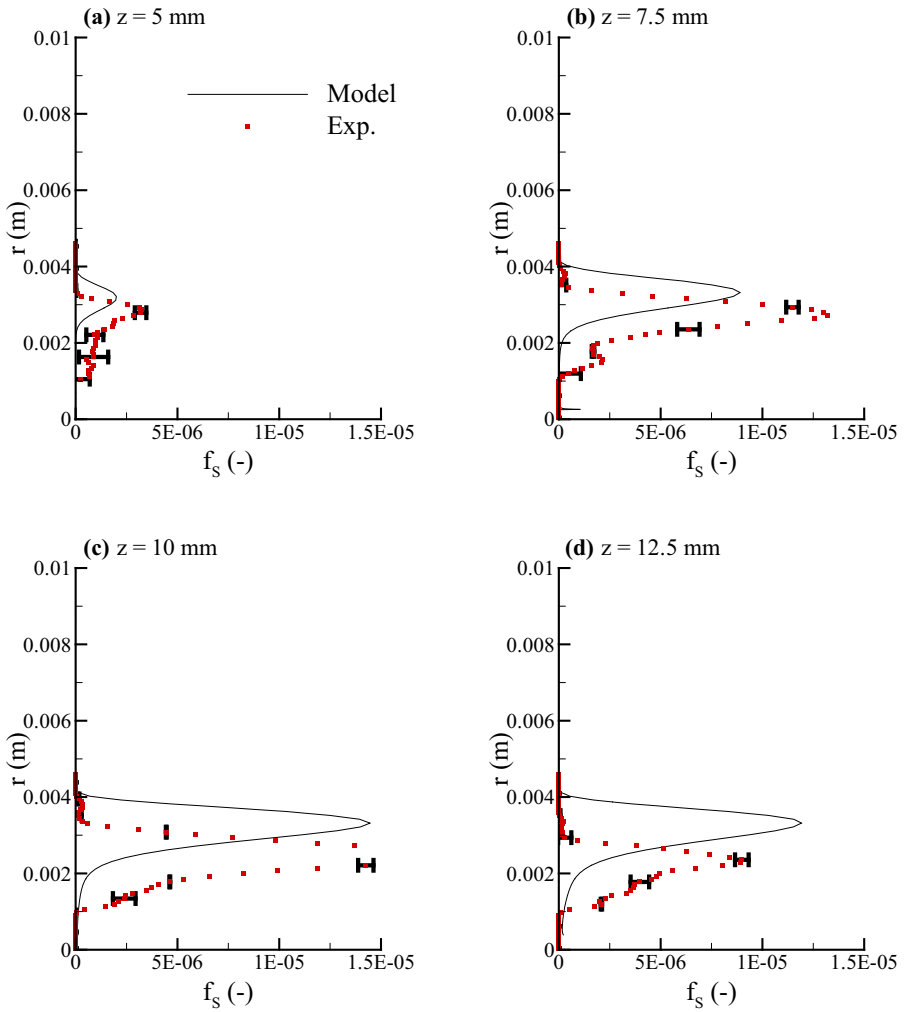


Figure 7. Computed and experimental radial profiles of soot volume fraction at different locations z along the wire: (a) $z = 5$ mm, (b) $z = 7.5$ mm, (c) $z = 10$ mm, and (d) $z = 12.5$ mm.

the peak of the soot oxidation rate by OH radicals. Figure 9 shows that both computed and measured evolutions of the stand-off distance along the wire are consistent. The stand-off distance increases up to $z \approx z_b = 5.8$ mm, remains approximately constant and then decreases. The start of the decreasing stage occurs for larger value of z in the calculations than in the experiments. These discrepancies explain at least partially that the predicted soot oxidation is less efficient than that observed experimentally (see Fig. 6). As expected, the definition of

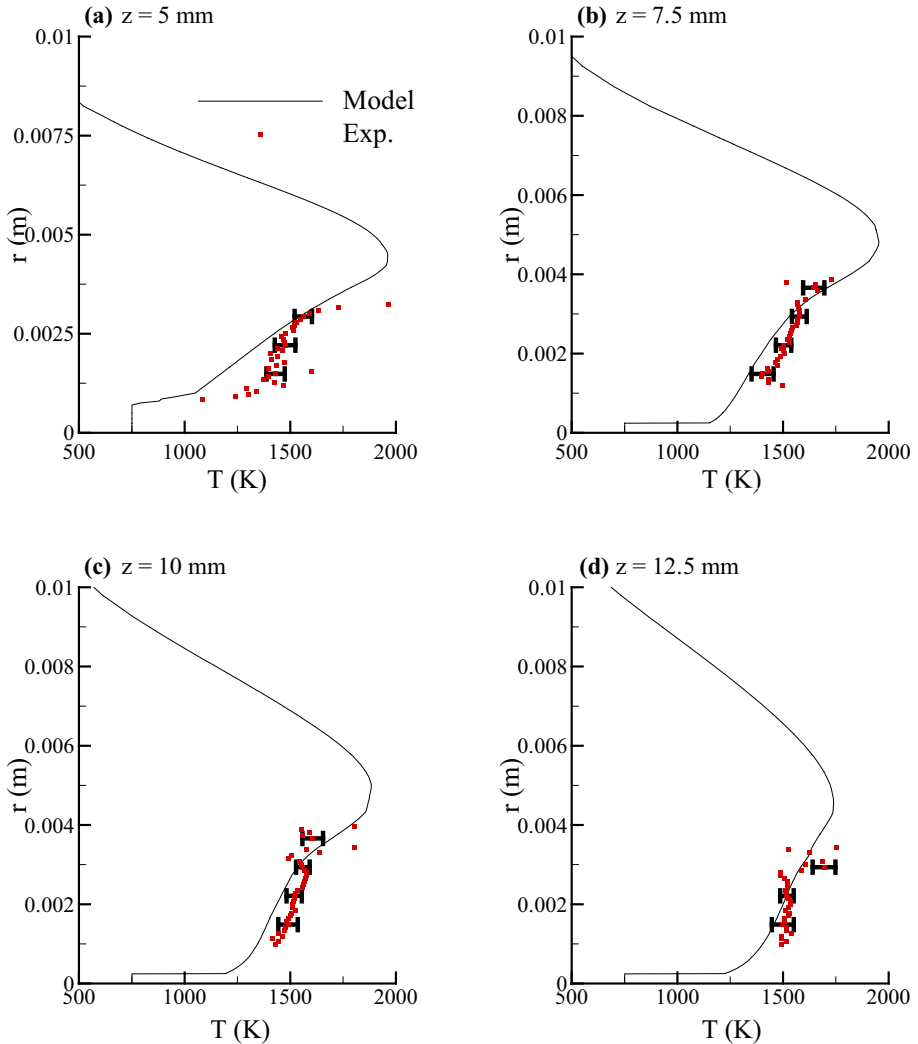


Figure 8. Computed and experimental radial profiles of temperature at different locations z along the wire: (a) $z = 5$ mm, (b) $z = 7.5$ mm, (c) $z = 10$ mm, and (d) $z = 12.5$ mm.

the stand-off distance based on the peak of the oxidation rate by OH is more consistent with the experimental one and provides a better agreement with the experimental data.

4.2. Radiative Heat Transfer

Figure 10 shows the incident radiative flux along the wire obtained with the complete radiation model described in Sect. 3.3.3. It is referred as complete in the

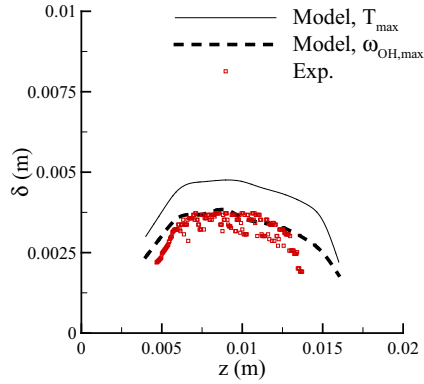


Figure 9. Stand-off distance as a function of the distance along the wire. The legend Model, T_{max} and Model, $\omega_{OH,max}$ indicate that the numerical stand-off distance is determined from the maximum temperature or the maximum soot oxidation by OH radical, respectively.

legend of Fig. 10. The molten ball region experiencing pyrolysis ($0 < z < z_b$) can be divided into two parts: (1) the region located downstream the highest value of r_b ($z_{b,max} < z < z_b$ with $z_{b,max}$ defined in Fig. 10) which is exposed directly to the flame radiation. As a consequence, a part of this region is exposed to relatively high radiative flux that reaches a peak of about 17.5 kW/m^2 at the vicinity of z_b and decreases up to 3.3 kW/m^2 at $z = z_{b,max}$; (2) the region located upstream $z_{b,max}$ ($0 < z < z_{b,max}$) which is partially hidden from the flame radiation and where the incident heat flux decreases rapidly to reach 1.12 kW/m^2 at $z = 0$. Along the

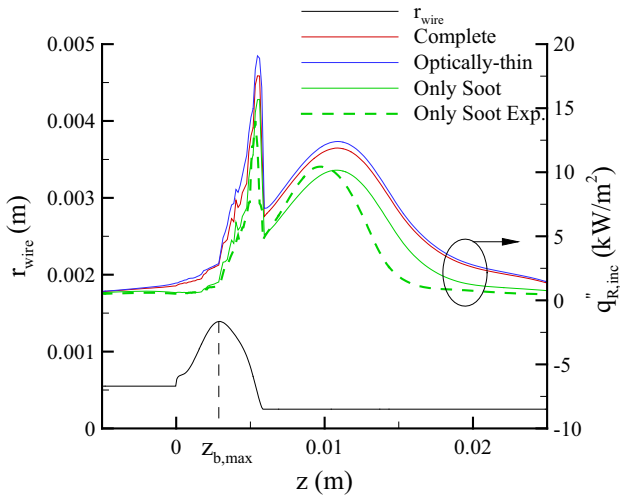


Figure 10. Incident radiative flux (right y-axis) along the wire. The axial evolution of the wire radius is also plotted (left y-axis).

region located upstream the molten ball ($z < 0$), the unburnt coated wire is exposed to modest incident radiative flux lower than 1.12 kW/m^2 . In contrast, along the bare wire ($z > z_b$), the incident radiative heat flux reaches a maximum of about 12 kW/m^2 at $z_{max} = 10 \text{ mm}$ which corresponds to the location of maximum soot volume fraction (see Fig. 6). The incident heat flux decreases rapidly as the distance from z_{max} increases. Table 4 shows that the radiant fraction, i.e. the part of the heat release rate radiated away from the flame, is 25.2% in this case.

Decoupled radiation calculations were run by neglecting self-absorption with the same thermal input (temperature, mole fraction of radiatively participating gaseous species, soot volume fraction) as for the complete case. The corresponding incident flux are denoted optically-thin in Fig. 10 and Table 4. The optically-thin approximation has negligible but noticeable effects on both radiant fraction and incident heat flux. Applying this approximation increases the radiant fraction by 3% and the peaks of incident radiative flux at $z \approx z_b$ and $z \approx 10.0 \text{ mm}$ by less than 5%.

Decoupled radiation calculations were also run by considering only soot radiation, i.e. by neglecting the contributions of CO_2 and H_2O . These calculations were run with the computed (denoted Only Soot) and the experimental (denoted Only Soot Exp.) fields of temperature and soot volume fraction. Table 4 shows that the radiant fraction computed by considering only soot radiation is equal to 0.167. This value has to be compared with the radiant fraction obtained with the complete model. This shows that soot radiation represents about 2/3 of the total radiation and, as such, prevails widely over gas radiation for the flame under consideration. As expected, the incident radiative flux computed by neglecting gas radiation is lower than that predicted by using the complete radiation model. It is also interesting to note that this approximation reduces significantly the predicted incident heat flux along the pyrolysing region located upstream $z_{b,max}$ ($0 < z < z_{b,max}$). Comparing the cases “Only Soot” and “Only Soot Exp.” in Fig. 10 reflects the effects of the discrepancies of the predicted soot volume fraction and temperature on the predicted incident radiative flux. It can be observed that the largest discrepancies are observed along the bare wire. The incident heat fluxes predicted with computed and measured fields of temperature and soot volume fraction are on the whole in good agreement, especially along the molten ball.

Table 4
Radiant Fractions for the Different Cases Investigated

Case	Complete	No soot	Optically-thin
χ_R	0.252	0.167	0.260

The case Complete takes both radiant gases and soot radiation into account, the case No Soot neglects the soot contribution and the case Optically-thin neglects gas and soot self-absorption

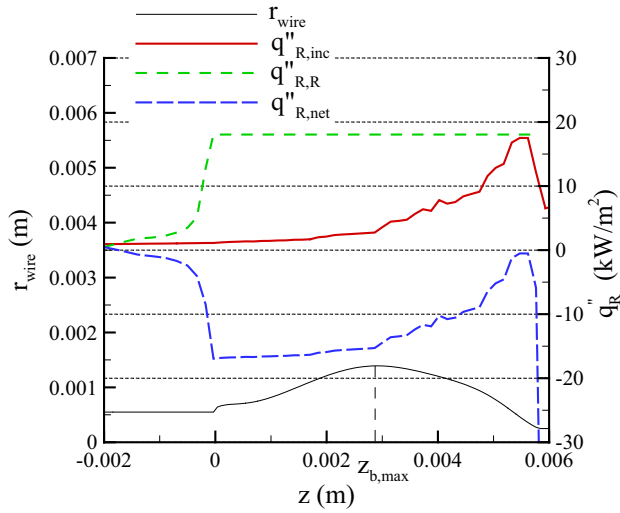


Figure 11. Incident, surface re-emission and net radiative fluxes (right y-axis) along the wire. The axial evolution of the wire radius is also plotted (right y-axis).

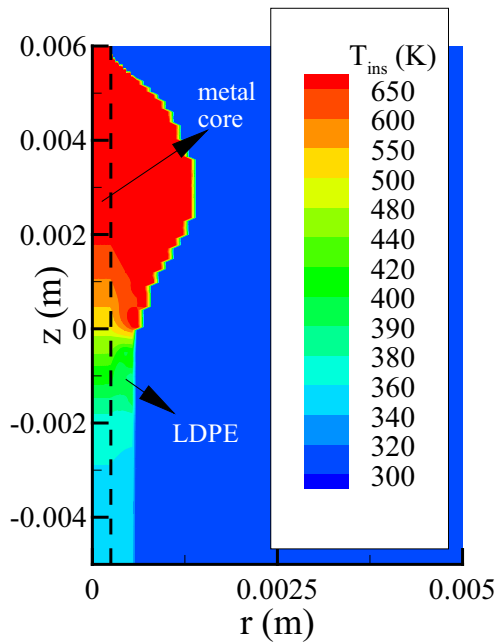


Figure 12. Computed temperature inside the condensed phase. The black dotted line indicates the frontier between the metallic core (left) and the LDPE coating (right).

4.3. Heat Transfer Toward the Pyrolysing Surface and Ahead of the Pyrolysis Front

Figure 11 shows $\dot{q}_{R,inc}''$, $\dot{q}_{R,R}''$ and the net radiative heat flux, defined as $\dot{q}_{R,net}'' = \dot{q}_{R,inc}'' - \dot{q}_{R,R}''$, along the molten ball surface and ahead of the ball leading edge. At each location, $\dot{q}_{R,R}''$ is significantly higher than $\dot{q}_{R,inc}''$. As a consequence, in these regions, the net radiative contribution to heat transfer to the surface, $\dot{q}_{R,net}''$, is negative. This suggests that the pyrolysis process is governed by the convective heat transfer from the flame whereas the heat flux ahead of the molten ball is controlled by the combined contribution of the convective heat flux and conductive heat transfer inside the condensed phase. This latter point is sustained by Fig. 12 that shows the temperature field inside the condensed material. This figure illustrates the importance of the conductive flux ahead of the molten ball inside the metal core. In addition, it shows that the thermally-thin assumption for the LDPE, widely used in previous studies (see Ref. [16] for example), is not fully valid.

5. Conclusions

Soot production and radiative heat transfer were experimentally and numerically investigated in opposed flame spread over a Nickel–Chrome wire coated with LDPE in microgravity under an oxygen content of 19%. The following conclusions can be drawn from the present study:

1. The numerical model reproduces correctly the available experimental data in terms of soot volume fraction, soot temperature, and stand-off distance. These results support the approximation of assimilating the pyrolysis products of LDPE to pure ethylene and demonstrate that the acetylene-benzene based soot model can be extended to polyethylene with minor modifications.
2. For the flame under consideration, soot radiation prevails over gas phase radiation and the optically-thin approximation is valid. Further investigations should be made to characterize flame radiation, especially those near the extinction limits.
3. The surface re-radiation along the pyrolysing surface and the virgin LDPE is higher than the incident radiative flux from the flame, leading to a negative net radiative flux. This shows that the convective heat transfer from the flame sustains the pyrolysis process and the flame spread is ensured owing to the combined contribution of convection from the flame and conduction inside the condensed material.
4. Model results show that the thermally-thin assumption throughout the LDPE coating is not strictly valid.

Acknowledgements

The authors feel grateful to the Centre National d'Etudes Spatiales for its financial support under Contract No. 130615.

References

1. Greenberg PS, Sacksteder KR, Kashiwagi T (1994) The USML-1 wire insulation flammability glovebox experiment. In: Third international microgravity combustion workshop 2, NASA Lewis Research Center, Cleveland, Ohio, pp 25–30
2. Kikuchi M, Fujita O, Ito K, Sato A, Sakuraya T (1998) Experimental study on flame spread over wire insulation in microgravity. *Proc Combust Inst* 27:2507–2514. [https://doi.org/10.1016/S0082-0784\(98\)80102-1](https://doi.org/10.1016/S0082-0784(98)80102-1)
3. Fujita O, Nishizawa K, Ito K (2002) Effect of low external flow on flame spread over polyethylene-insulated wire in microgravity. *Proc Combust Inst* 29:2545–2552. [https://doi.org/10.1016/S1540-7489\(02\)80310-8](https://doi.org/10.1016/S1540-7489(02)80310-8)
4. Citerne JM, Dutilleul H, Kizawa K, Nagachi M, Fujita O, Kikuchi M, Jomaas G, Rouvreau S, Torero JL, Legros G (2016) Fire safety in space—investigating flame spread interaction over wires. *Acta Astronaut* 126:500–509. <https://doi.org/10.1016/j.actaastro.2015.12.021>
5. Osorio AF, Mizutani K, Fernandez-Pello C, Fujita O (2015) Microgravity flammability limits of ETFE insulated wires exposed to external radiation. *Proc Combust Inst* 35:2683–2689. <https://doi.org/10.1016/j.proci.2014.09.003>
6. Longhua H, Yong L, Yoshioka K, Yangshu Z, Fernandez-Pello C, Ho CS, Fujita O (2017) Limiting oxygen concentration for extinction of upward spreading flames over inclined thin polyethylene-insulated NiCr electrical wires with opposed-flow under normal- and micro-gravity. *Proc Combust Inst* 36:3045–3053. <https://doi.org/10.1016/j.proci.2016.09.021>
7. Kong W, Liu F (2009) Numerical study of the effects of gravity on soot formation in laminar coflow methane/air diffusion flames under different air stream velocities. *Combust Theory Model* 13:993–1023. <https://doi.org/10.1080/13647830903342527>
8. Contreras J, Consalvi JL, Fuentes A (2018) Numerical simulations of microgravity ethylene/air laminar boundary layer diffusion flames. *Combust Flame* 191:99–108. <https://doi.org/10.1016/j.combustflame.2017.12.013>
9. Takahashi S, Kondou M, Wakai K, Bhattacharjee S (2002) Effect of radiation loss on flame spread over a thin PMMA sheet in microgravity. *Proc Combust Inst* 29:2579–2586. [https://doi.org/10.1016/S1540-7489\(02\)80314-5](https://doi.org/10.1016/S1540-7489(02)80314-5)
10. Legros G, Joulain P, Vantelon JP, Fuentes A, Bertheau D, Torero JL (2006) Soot volume fraction measurements in a three-dimensional laminar diffusion flame established in microgravity. *Combust Sci Technol* 178:813–835. <https://doi.org/10.1080/00102200500271344>
11. Fuentes A, Rouvreau S, Joulain P, Vantelon JP, Legros G, Torero JL, Fernandez-Pello C (2007) Sooting behavior dynamics of a non-buoyant laminar diffusion flame. *Combust Sci Technol* 179:3–19. <https://doi.org/10.1080/00102200600805850>
12. Fuentes A, Legros G, Claverie A, Joulain P, Vantelon JP, Torero JL (2007) Interactions between soot and CH radicals in a laminar boundary layer type diffusion flame in microgravity. *Proc Combust Inst* 31:2685–2692. <https://doi.org/10.1016/j.proci.2006.08.031>

13. Legros G, Fuentes A, Rouvreau S, Joulain P, Porterie B, Torero JL (2009) Transport mechanisms controlling soot production inside a non-buoyant laminar diffusion flame. *Proc Combust Inst* 32:2461–2470. <https://doi.org/10.1016/j.proci.2008.06.179>
14. Legros G, Torero JL (2015) Phenomenological model of soot production inside a non-buoyant laminar diffusion flame. *Proc Combust Inst* 35:2545–2553. <https://doi.org/10.1016/j.proci.2014.05.038>
15. Contreras J, Consalvi JL, Fuentes A (2017) Oxygen index effect on the structure of a laminar boundary layer diffusion flame in a reduced gravity environment. *Proc Combust Inst* 36:3237–3245. <https://doi.org/10.1016/j.proci.2016.06.065>
16. Takahashi S, Takeuchi H, Ito H, Nakamura Y, Fujita O (2013) Study on unsteady molten insulation volume change during flame spreading over wire insulation in micro-gravity. *Proc Combust Inst* 34:2657–2664. <https://doi.org/10.1016/j.proci.2012.06.158>
17. Guibaud A, Citerne JM, Orlac'h JM, Fujita O, Consalvi JL, Torero JL, Legros G (2018) Broadband modulated absorption/emission technique to probe sooting flames: implementation, validation, and limitations. *Proc Combust Inst*. <https://doi.org/10.1016/j.proci.2018.06.199>
18. Ferkul P, Sacksteder K, Greenberg P, Dietrich D, Ross H, Tien JS, Altenkirch R, Tang L, Bundy M, Delichatsios M Combustion experiments on the Mir Space Station. AIAA-99-0439. <https://doi.org/10.2514/6.1999-439>
19. Emmons HW (1956) The film combustion of liquid fuel. *Z für Angew Math Mech* 36:60–71
20. Consalvi JL, Porterie B, Loraud JC (2005) A blocked-off region strategy to compute fire scenarios involving internal flammable targets. *Numer Heat Trans* 47:419–441. <https://doi.org/10.1080/10407790590919234>
21. Zhang J, Wang Y, Lu X (2005) Study on melting behavior of polymers during burning. *Fire Saf Sci* 8:637–646. <https://doi.org/10.3801/IAFSS.FSS.8-637>
22. Gauthier E, Laycock B, Cuoq FJJM, Halley PJ, George KA (2012) Correlation between chain microstructural changes and embrittlement of LLDPE-based films during photo- and thermo-oxidative degradation. *Polym Degrad Stab*. <https://doi.org/10.1016/j.polymdegradstab.2012.08.021>
23. Guo H, Liu F, Smallwood GJ, Gülder ÖL (2006) Numerical study on the influence of hydrogen addition on soot formation in a laminar ethylene-air diffusion flame. *Combust Flame* 145:324–338. <https://doi.org/10.1016/j.combustflame.2005.10.016>
24. Khan MM, Tewarson A, Chaos M (2016) Combustion characteristics of materials and generation of fire products. In: Hurley MJ (ed) *SFPE handbook of fire protection engineering*, 5th edn. Springer, New York, pp 1143–1232
25. Annamalai K, Sibulkin M (1979) Flame spread over combustible surfaces for laminar flow systems part I: excess fuel and heat flux. *Combust Sci Technol* 19:167–183
26. Rangwala AS (2016) Diffusion flames. In: Hurley MJ (ed) *SFPE handbook of fire protection engineering*, 5th edn. Springer, New York, pp 350–372
27. Qin Z, Lissianski VV, Yang H, Gardiner WC, Scott SG, Wang H (2000) Combustion chemistry of propane: a case study of detailed reaction mechanism optimization. *Proc Combust Inst* 28:1663–1669. [https://doi.org/10.1016/S0082-0784\(00\)80565-2](https://doi.org/10.1016/S0082-0784(00)80565-2)
28. Lindstedt RP (1994) Simplified soot nucleation and surface growth steps for non-premixed flames. In: Bockhorn H (ed) *Soot formation in combustion* Springer, Berlin, pp 417–441
29. Nmira F, Consalvi JL, Demarco R, Gay L (2015) Assessment of semi-empirical soot production models in C_1 – C_3 axisymmetric laminar diffusion flames. *Fire Saf J* 73:79–92. <https://doi.org/10.1016/j.firesaf.2015.03.005>

30. Moss JB, Aksit IM (2007) Modelling soot formation in a laminar diffusion flame burning a surrogate kerosene fuel. *Proc Combust Inst* 31:3139–3146. <https://doi.org/10.1016/j.proci.2006.07.016>
31. Naggle J, Strickland-Constable RF (1962) Oxidation of carbon between 1000°C and 2000°C. In: *Proceedings of the 5th conference on carbon*. Pergamon Press, London, pp 154–164
32. Fenimore CP, Jones GW (1967) Oxidation of soot by hydroxyl radicals. *J Phys Chem* 71:593–597. <https://doi.org/10.1021/j100862a021>
33. Rothman LS, Gordon IE, Barber RJ, Dothe H, Gamache RR, Goldman A, Perevalov VI, Tashkun TJ (2010) HITEMP: the high-temperature molecular spectroscopic database. *J Quant Spectrosc Radiat Transf* 111:2139–2150. <https://doi.org/10.1016/j.jqsrt.2010.05.001>
34. Chang H, Charalampopoulos T (1990) Determination of the wavelength dependence of refractive indices of flame soot. *Proc R Soc* 430:577–591. <https://doi.org/10.1098/rspa.1990.0107>
35. Modest MF, Zhang H (2002) The full-spectrum correlated-k distribution for thermal radiation from molecular gas-particulate mixtures. *ASME J Heat Transf* 124:30–38. <https://doi.org/10.1115/1.1418697>
36. Modest MF (2003) *Radiative heat transfer*. Academic Press, London
37. Modest MF, Riazzi RJ (2005) Assembly full spectrum k-distribution from a narrow band database: effects of mixing gases, gases and non-gray absorbing particles and non-gray scatters in non-gray enclosures. *J Quant Spectrosc Radiat Transf* 90:169–189. <https://doi.org/10.1016/j.jqsrt.2004.03.007>
38. Chui EH, Raithby GD, Hughes PMJ (1992) Prediction of radiative transfer in cylindrical enclosures with the finite volume method. *AIAA J Thermophys Heat Transf* 6:605–611. <https://doi.org/10.2514/3.11540>
39. Chen CH, T'ien JS (2007) Diffusion flame stabilization at the leading edge of a fuel plate. *Combust Sci Technol* 179:3–19. <https://doi.org/10.1080/00102208608923938>
40. Markstein GH, De Ris J (1985) Radiant emission and absorption by laminar ethylene and propylene diffusion flames. *Proc Combust Inst* 20:1637–1646. [https://doi.org/10.1016/S0082-0784\(85\)80659-7](https://doi.org/10.1016/S0082-0784(85)80659-7)
41. Kent JH (1986) A quantitative relationship between soot yield and smoke point measurements. *Combust Flame* 63:349–358. [https://doi.org/10.1016/0010-2180\(86\)90004-0](https://doi.org/10.1016/0010-2180(86)90004-0)

Publisher's Note Springer Nature remains neutral with regard to jurisdictional claims in published maps and institutional affiliations.